Available online at www.sciencedirect.com
ScienceDirect
Trans. Nonferrous Met. Soc. China 32(2022) 3873−3886
Transactions of Nonferrous Metals Society of China
www.tnmsc.cn

Simulation of strain induced abnormal grain growth in aluminum alloy by coupling crystal plasticity and phase field methods

Ru-xue LIU[1], Kai LI[1], Guo-wei ZHOU[2], Wei-qin TANG[1], Yao SHEN[3], Ding TANG[1], Da-yong LI[1]

1. School of Mechanical Engineering, Shanghai Jiao Tong University, Shanghai 200240, China;
2. School of Naval Architecture, Ocean and Civil Engineering,
Shanghai Jiao Tong University, Shanghai 200240, China;
3. School of Materials Science and Engineering, Shanghai Jiao Tong University, Shanghai 200240, China

Received 7 September 2021; accepted 21 April 2022

Abstract: A mesoscale modeling methodology is proposed to predict the strain induced abnormal grain growth in the annealing process of deformed aluminum alloys. Firstly, crystal plasticity finite element (CPFE) analysis is performed to calculate dislocation density and stored deformation energy distribution during the plastic deformation. A modified phase field (PF) model is then established by extending the continuum field method to consider both stored energy and local interface curvature as driving forces of grain boundary migration. An interpolation mapping approach is adopted to transfer the stored energy distribution from CPFE to PF efficiently. This modified PF model is implemented to a hypothetical bicrystal firstly for verification and then the coupled CPFE−PF framework is further applied to simulating the 2D synthetic polycrystalline microstructure evolution in annealing process of deformed AA3102 aluminum alloy. Results show that the nuclei with low stored energy embedded within deformed matrix tend to grow up, and abnormal large grains occur when the deformation is close to the critical plastic strain, attributing to the limited number of recrystallized nuclei and inhomogeneity of the stored energy.

Key words: abnormal grain growth; stored deformation energy; recrystallization; crystal plasticity; phase field

1 Introduction

Static recrystallization (SRX) occurs in post-deformation annealing and grain growth takes place after the primary recrystallization [1]. The grain growth is typically categorized as normal grain growth (NGG) [2] and abnormal grain growth (AGG) [3]. The grain size remains uniform during NGG, while in AGG, a few grains with remarkably higher boundary migration velocities grow abnormally at the expense of fine matrix, leading to a bimodal grain size distribution. AGG has been reported in many polycrystalline materials [3−10] and is one of the most undesirable cases due to the significant degradation of mechanical properties, e.g. strength, stress corrosion resistance and fracture toughness. The underlying mechanisms of AGG have been reported to correlate with various factors, e.g. texture [4], boundary properties [5], pre-strain [6], recrystallization [7,8] and dissolving or low density of particles [9,10], all of which are closely in connection with strain induced grain boundary migration (SIBM).

The applied work during deformation is partly converted into heat and dissipated, while a small portion remains as stored deformation energy in the form of dislocation structures. Various factors, such as grain orientations, grain boundary as well

Corresponding author: Guo-wei ZHOU, Tel: +86-15216717318, E-mail: zgw99@sjtu.edu.cn;
Wei-qin TANG, Tel: +86-13402117220, E-mail: weiqint@sjtu.edu.cn
DOI: 10.1016/S1003-6326(22)66064-3

as second particles, can induce inhomogeneity of stored deformation energy among grains. This inhomogeneity has remarkable effects on the later microstructure evolution in annealing since the grain boundary mobility is mainly driven by two driving forces, i.e. local boundary curvature and stored energy [11]. The curvature driving force propels a grain boundary segment towards its center of curvature in order to reduce the entire boundary energy, while SIBM is regarded as the movement of grain boundary driven by the stored energy difference across that boundary segments. Particularly, AGG can be promoted as a few recrystallization nuclei with low stored energy growing into abnormally large grains due to the heterogeneous residual strain produced in the previous deformation [7,12].

To provide more detailed information from the mechanism aspect, different simulation frameworks have been proposed to model the mechanical response and microstructural evolution (e.g. nucleation and grain growth) in the complex processes of both deformation and annealing. The accurate grain level deformation prediction is the base of annealing simulation, and the crystal plasticity theory based on the slip deformation mechanism is widely adopted to simulate the plastic deformation in a polycrystalline representative volume element (RVE) [13]. The stress and strain within grains and their orientation dependence can be predicted in consideration of inter grain equilibrium and compatibility. Incorporating the dislocation density-based hardening models with crystal plastic finite element (CPFE) method provides a feasible way to evaluate the evolution of dislocation density and stored deformation energy under various loading conditions [14−16].

There are also several mesoscale methods for the microstructure evolution predictions in heat treatment process, for example, cellular automation (CA) [17], Monte Carlo (MC) [18], and phase field (PF) [19−22], among which the PF established upon the diffuse interface description of the grain boundary plays a critical role in the annealing simulation and does not need to track the moving boundary explicitly. Three main types of PF methods are widely used to study grain growth in polycrystalline materials: (1) KWC (proposed by KOBAYASHI, WARREN and CRAIG CARTER) [19]; (2) multi-phase field (MPF) [20]; (3) continuum field (CF) [21,22]. In KWC, a single field variable is applied to representing the orientation distribution of all grains, while various field variables are required in MPF and CF. The sum of the phase field variables for a single point in MPF, which are interpreted as volume fractions, must be equal to 1, while they are treated independently in CF.

Many simulation studies are conducted to model the plasticity-induced microstructure evolution by combining phase field with crystal plasticity methods. ABRIVARD et al [23] established KWC phase field-crystal plasticity framework to describe the kinetics of grain boundary migration driven by curvature and local stored energy gradients associated with inelastic deformation. GÜVENÇ et al [24] proposed a coupled CPFE and MPF method and mimicked the main features of the SRX. TAKAKI and TOMITA [25] developed a CPFE−MPF coupled model to simulate recrystallization after different compression strains by taking the inhomogeneity of the plastic deformation of a polycrystalline metal into account. A mesoscale continuum theory was developed by JAFARI et al [11,26] based on the coupling of CPFE and PF methods to describe the SIBM driven by the heterogeneity of stored deformation energy in a plastically deformed polycrystalline cubic metal. However, the deformation within each grain is considered to be homogeneous in their work. The intra-granular heterogeneous dislocation density has been neglected in microstructure evolution predictions. Moreover, very little simulation work has been conducted to couple crystal plasticity with CF phase filed method. ZHAO et al [27] developed a computational tool to simulate dynamic SIBM in copper through concurrent coupling of CPFE and CF models, but only a bicrystal configuration with straight grain boundaries was tested and there was no further application in polycrystalline microstructure.

In current work, a novel crystal plasticity-phase field coupled framework is proposed to model the deformation and the following strain induced grain growth of aluminum alloy. The dislocation density-based CPFE model predicts both the inter and intra-granularly heterogeneous dislocation densities, and the modified CF model is extended by incorporating both the interface curvature and stored deformation energy as driving

forces of grain growth. An interpolation mapping method is adopted to transfer the stored energy distribution from CPFE to PF efficiently. The modified PF model is implemented on a hypothetical bicrystal firstly for verification, and then the coupled CPFE−PF framework is further applied to simulating the 2D synthetic poly-crystalline microstructure evolution (AGG in particular) in annealing process of deformed AA3102 aluminum alloy.

2 Simulation framework

2.1 Crystal plasticity formulation

In order to predict the heterogeneous deformation in each grain at the mesoscale, the elasto-viscoplastic crystal plasticity framework proposed by MARIN and DAWSON [28] is adopted and applied with finite element code to simulate the deformation of grain aggregate. In current work, each grain is modeled with multiple elements, and the deformation gradient $\boldsymbol{F}$ at each material point is decomposed as

$$\boldsymbol{F}=\boldsymbol{F}^{\mathrm{e}}\boldsymbol{F}^{\mathrm{p}} \tag{1}$$

where $\boldsymbol{F}^{\mathrm{p}}$ is the plastic part (dislocation slip) of deformation gradient matrix and $\boldsymbol{F}^{\mathrm{e}}$ is the elastic part (lattice strain and rotation) of the deformation gradient matrix.

The plastic deformation gradient is calculated from the flow rule as follows:

$$\dot{\boldsymbol{F}}^{\mathrm{p}}(\boldsymbol{F}^{\mathrm{p}})^{-1}=\sum_{\alpha=1}^{N}\dot{\gamma}^{\alpha}\boldsymbol{m}^{\alpha}\otimes\boldsymbol{n}^{\alpha} \tag{2}$$

where $\dot{\gamma}$ is the shear strain rate, $\boldsymbol{m}$ and $\boldsymbol{n}$ are the slip direction and the slip plane normal vectors of α slip system, respectively, and N is the number of slip systems.

The constitutive equation for a single crystal is given with Green−Lagrange strain tensor ($\boldsymbol{E}^{\mathrm{e}}$) and its work conjugate second Piola−Kirchhoff stress tensor ($\boldsymbol{S}$):

$$\boldsymbol{E}^{\mathrm{e}}=[(\boldsymbol{F}^{\mathrm{e}})^{\mathrm{T}}\boldsymbol{F}^{\mathrm{e}}-\boldsymbol{I}]/2 \tag{3}$$

$$\boldsymbol{S}=\boldsymbol{C}\boldsymbol{E}^{\mathrm{e}} \tag{4}$$

where $\boldsymbol{C}$ denotes fourth order elasticity tensor and I is a unit matrix.

The phenomenological power law proposed by HUTCHINSON [29] is used to calculate the shear strain rate ($\dot{\gamma}^{\alpha}$) on α slip system with resolved shear stress (τ^{α}):

$$\dot{\gamma}^{\alpha}=\dot{\gamma}_0\left|\tau^{\alpha}/\tau_{\mathrm{C}}^{\alpha}\right|^{1/m}\mathrm{sgn}(\tau^{\alpha}) \tag{5}$$

where $\dot{\gamma}_0$ is a reference shear strain rate, m is the strain rate sensitivity, and $\tau_{\mathrm{C}}^{\alpha}$ is the critical resolved shear stress (CRSS). In current simulation, for aluminum alloys, $\dot{\gamma}_0$=1.0 s^{-1} and m=0.05 are adopted.

In the plastic deformation of Al alloy, the slip resistance/critical resolved shear stress is determined by the dislocation density on each slip system. The corresponding dislocation density evolution is governed by its generation and annihilation, which can be described by the model proposed by KOCKS and MECKING [30]:

$$\frac{\partial\rho^{\alpha}}{\partial\gamma^{\alpha}}=k_1\sqrt{\rho^{\alpha}}-k_2(\dot{\varepsilon},T)\rho^{\alpha} \tag{6}$$

where k_1 is a material constant of work hardening, ρ is the dislocation density, and k_2 represents the effects of the dynamic recovery and is a function of k_1, temperature T and strain rate $\dot{\varepsilon}$ [31]. The details of parameters determination (k_1, k_2) are given in Appendix.

The related CRSS is calculated with a simplified equation in which only the initial slip resistance (τ_0^{α}), and the resistance encountered from forest dislocations by the gliding dislocation are considered [32]:

$$\tau_{\mathrm{C}}^{\alpha}=\tau_0^{\alpha}+\tau_{\mathrm{forest}}^{\alpha} \tag{7}$$

where $\tau_{\mathrm{forest}}^{\alpha}=b\chi\mu\sqrt{\rho^{\alpha}}$, χ represents an interaction factor and is assigned with 1 in this work, b is the amplitude of Burgers vector (2.86×10^{-10} m for Al), and μ is the shear modulus (26.1 GPa for Al at room temperature).

The crystal plasticity model was implemented as a user subroutine (UMAT) within ABAQUS/standard platform, following the procedure outlined in MARIN and DAWSON [28].

2.2 Modified phase field algorithm

In the model developed by FAN and CHEN [22], a set of continuous field variables were used to represent different grains. For example, a polycrystalline volume of N_{g} grains is represented by N_{g} field variables. Each phase field variable or structural variable represents a particular structure unit with a specific single crystal orientation.

Within the grain labeled with i, the order parameter η_i equals 1 and the rest η_j ($j\neq i$) equals 0. At grain boundary, the η_i varies continually from 1 to 0. The total free energy F as a functional of the phase field variables and their gradients of the poly-crystalline system can be written as

$$F=\int_V\left[m_{\mathrm{p}}f\left(\eta_1,\ \eta_2,\ \cdots,\ \eta_{N_{\mathrm{g}}}\right)+\sum_i^{N_{\mathrm{g}}}\frac{\kappa_i}{2}|\nabla\eta_i|^2\right]\mathrm{d}V \tag{8}$$

where f is the free energy density of the grains with a constant coefficient of m_{p}; N_{g} is the number of grains in the system; κ_i is the energy gradient coefficient; V represents the computational domain; $\mathrm{d}V$ is the infinitesimal in the domain.

The following free energy density expression is proposed by CHEN and YANG [21]:

$$f\left(\eta_1,\ \eta_2,\ \cdots,\ \eta_{N_{\mathrm{g}}}\right)=\sum_i^{N_{\mathrm{g}}}\left(-\frac{A}{2}\eta_i^2+\frac{B}{4}\eta_i^4\right)+w_{ij}\sum_i^{N_{\mathrm{g}}}\sum_{i\neq j}^{N_{\mathrm{g}}}\eta_i^2\eta_j^2 \tag{9}$$

where A, B and w_{ij} are positive constants in free energy function.

The stored deformation energy (ψ_i) within the deformed microstructure can be evaluated by a function of dislocation density [33]:

$$\psi_i=\alpha_E\mu b^2\sum_{\alpha=1}^{N}\rho_i^{\alpha} \tag{10}$$

where α_E is a constant and assigned with 0.5 in the present work.

In this work, the stored deformation energy term (ψ) is added in the free energy function:

$$F=\int_V[m_{\mathrm{p}}f\left(\eta_1,\ \eta_2,\ \cdots,\ \eta_{N_{\mathrm{g}}}\right)+\sum_i^{N_{\mathrm{g}}}\frac{\kappa_i}{2}|\nabla\eta_i|^2+C_{\mathrm{s}}\psi]\mathrm{d}V \tag{11}$$

where C_{s} is the spatial scale-related matching coefficient of stored energy.

For uniform grain boundary system, w_{ij} and $\kappa_{i,j}$ are both constant variables, $w_{ij}=W$ and $\kappa_{i,j}=\kappa$. As suggested by MOELANS et al [34], W=1.5 is an appropriate choice for grain growth simulation which can result in a symmetrical phase field profile for the grain boundary. In this case, the boundary energy (γ) is

$$\gamma=2\sqrt{m_{\mathrm{p}}\kappa(\frac{1}{2}+W)}\int_0^1\eta_i(1-\eta_i)\mathrm{d}\eta_i=\frac{\sqrt{2}}{3}\sqrt{m_{\mathrm{p}}\kappa} \tag{12}$$

The thickness of the grain boundary l_{gb} is

$$l_{\mathrm{gb}}=\sqrt{8\kappa/m_{\mathrm{p}}} \tag{13}$$

A proper grain boundary thickness is required as abnormal run of phase field simulation may occur when the distance between grid points in phase field model is larger than l_{gb}. In the present work, the following rule (Eq. (14)) is proposed to correct the thickness of the grain boundary by adjusting the value of boundry thickness factor C_{gb} without affecting the boundary energy:

$$\frac{\sqrt{2}}{3}C_{\mathrm{gb}}\sqrt{m_{\mathrm{p}}\kappa}=\frac{\sqrt{2}}{3}\sqrt{m_{\mathrm{p}}\kappa_0} \tag{14}$$

where κ_0 is the energy gradient coefficient without introducing C_{gb} into free energy function. Hence, the free energy function of phase field can be written as

$$F=\int_V[C_{\mathrm{gb}}(m_{\mathrm{p}}(\sum_i^{N_{\mathrm{g}}}\left(-\frac{A}{2}\eta_i^2+\frac{B}{4}\eta_i^4\right)+W\sum_i^{N_{\mathrm{g}}}\sum_{i\neq j}^{N_{\mathrm{g}}}\eta_i^2\eta_j^2)+\sum_i^{N_{\mathrm{g}}}\frac{\kappa}{2}|\nabla\eta_i|^2)+C_{\mathrm{s}}\psi]\mathrm{d}V \tag{15}$$

The evolution of order parameters with time follows Allen−Cahn dynamics:

$$\frac{\partial\eta_i(r,t)}{\partial t}=-L_i\frac{\delta F}{\delta\eta_i(r,t)},\ i=1,\ 2,\ \cdots,\ N_{\mathrm{g}} \tag{16}$$

where r is the point position in the field; t is the annealing time; L_i is the positive kinetic parameter.

In the present phase field model, phase transformation occurs only at the grain boundary. Based on Eqs. (14)−(16), the evolution of order parameters then can be further described as follows:

$$\frac{\partial\eta_i(r,t)}{\partial t}=-L_i\left[C_{\mathrm{gb}}(m_{\mathrm{p}}(-A\eta_i+B{\eta_i}^3+2W\eta_i\sum_{i\neq j}^{N_{\mathrm{g}}}\eta_j^2)-\kappa\nabla^2\eta_i)+C_{\mathrm{s}}\frac{\partial\psi}{\partial\eta_i(r,t)}\right] \tag{17}$$

The distances between grid points in 2D phase field model (Δx and Δy) should be balanced with both simulation precision and the computation cost. In present work, Δx and Δy are set in micrometer scale. The phase field model is coded with MATLAB software.

2.3 Phase field model verification with bicrystal case

The process of SIBM in aluminum alloy is

performed with a hypothetical bicrystal microstructure in this section to verify the phase field model. The velocity of grain boundary migration is determined by the driving force P_{gb} across the grain boundary [33]:

$$V_{gb}=M_{gb}P_{gb} \tag{18}$$

where M_{gb} is the grain boundary mobility factor and calculated as follows:

$$M_{gb}=M_0\exp[-Q/(RT)] \tag{19}$$

where M_0 is the pre-exponential factor; Q is the activation energy; R is the molar gas constant. Here, the material constants for aluminum alloy in annealing treatment at 600 °C are adopted from Ref. [26], M_0=1.23×10^4 m·s^{-1}·Pa^{-1}, Q=170 kJ·mol^{-1}, and R=8.314 J·mol^{-1}·K^{-1}. Then, the mobility factor of grain boundaries M_{gb} is obtained to be 8.27×10^{-7} m·s^{-1}·Pa^{-1}. P_{gb}, the net driving force for the migration of the grain boundary in a 2D configuration, can be given as [26]

$$P_{gb}=-\frac{\gamma}{R_i}+\Delta\psi \tag{20}$$

where the first term represents the driving force due to grain boundary curvature, R_i is the local radius of boundary curvature, and the second one, $\Delta\psi$, is due to the stored deformation energy difference across grain boundary. The average high angle grain boundary energy γ for aluminum is set to be 0.231 J/m^2 [35].

To clearly illustrate the grain boundary migration, a phase field model including two grains with straight migrating grain boundaries is shown in Fig. 1. The domain size is 248 μm × 124 μm, with grid spacing of 0.912 μm. The initial dislocation densities in Grain 1 and Grain 2 are 1×10^9 and 1×10^{14} m^{-2}, respectively. In this study, A=1; B=1; κ is fixed as 5×10^{-6} N; m_p=1×10^{-6} Pa; C_{gb}=0.219; l_{gb}=6.32 μm; C_s=3×10^{-6}. According to the derivation ($L\approx 4M_{gb}/3l_{gb}$) [34], there is L=0.175×10^{-6} Pa^{-1}·s^{-1}. Due to the existing deformation energy difference across the two grain boundaries, the grain boundaries will migrate along the directions as shown in Fig. 1 during the simulation. The driving force is 0.11 MPa, and there is no contribution from grain boundary curvature due to the infinite local radius (Eq. (20)). Grain 2 will be consumed gradually by Grain 1 with lower initial dislocation density, as shown in Fig. 1(b).

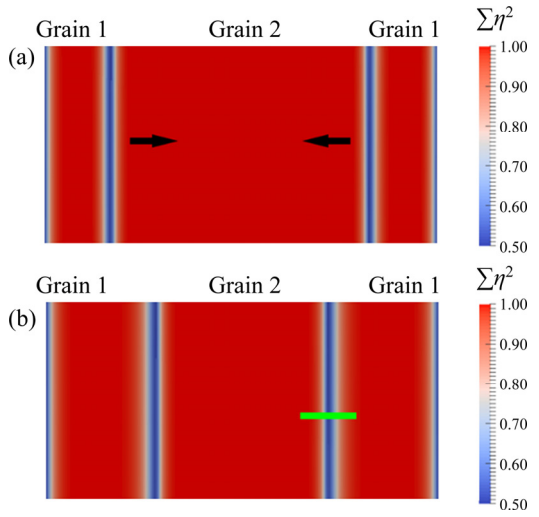

Fig. 1 Phase field model for bicrystal with straight boundaries: (a) Initial configuration; (b) Configuration during boundary migration

The filed variables across the grain boundaries, as marked with green line in Fig. 1(b), are further analyzed. The initial dislocation density difference across the boundary $\Delta\rho$ is set variously from 0 to 2×10^{14} m^{-2}. Two field variables η_i (η_2) and η_j (η_1) across the migrating boundary are plotted in Fig. 2. Zero distance represents the point at the middle of grain boundary. Figure 2 shows the grain boundary profiles with different $\Delta\rho$ across the boundary. When $\Delta\rho$=0, the curves of η_i and η_j are symmetrical near the middle of the boundary. But it turns to be asymmetrical when $\Delta\rho$ is larger than 0. The degree of asymmetry becomes more significant with increasing $\Delta\rho$.

According to Eq. (18), when the mobility factor M_{gb} is fixed, the migration velocity of the straight boundary V_{gb} is linearly related with the

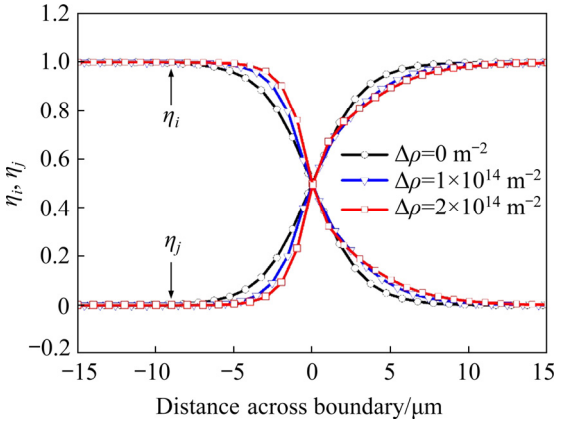

Fig. 2 Evaluation of η_i and η_j across grain boundary between Grains i and j

driving force P_{gb}. As shown in Fig. 2, in the present phase field model, the variety of stored energy difference results in different profiles of grain boundaries, leading to the migration velocity deviation from the prediction by Eq. (18). Thus, a correction factor R_C is introduced to correct the kinetic parameter:

$$L_i'=R_C L_i \tag{21}$$

The value of R_C can be determined by fitting results from the numerical simulations with various energy differences across the grain boundary. In the present aluminum alloy, the quantitative relationship between the stored energy difference across the boundary and the mobility correction factors (C_1, C_2, C_3) can be fitted by the following function:

$$R_C=C_1P_{gb}^2+C_2P_{gb}+C_3 \tag{22}$$

where C_1, C_2 and C_3 are constants in scale factor R_C and $C_1=4.688\times10^{-12}\ m^6\cdot J^{-2}$, $C_2=1.717\times10^{-6}\ m^3\cdot J^{-1}$, and $C_3=1.314$, as shown in Fig. 3.

After all the parameters are determined with the bicrystal model of straight boundaries, the established phase field model is further applied to a round grain growth simulation. As shown in Fig. 4,

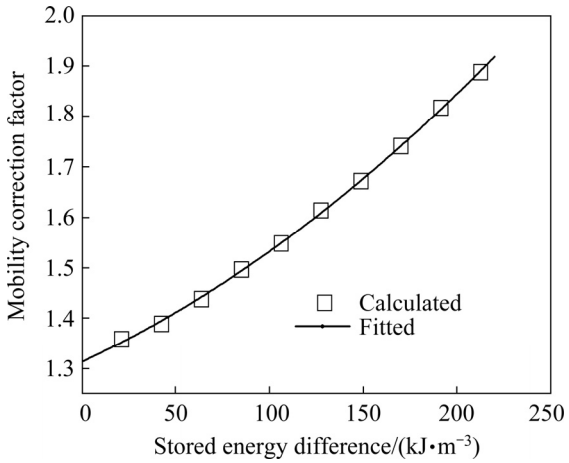

Fig. 3 Function relationship between mobility correction factor and stored energy difference

a small grain with radius of 20 μm is embedded in a square grain matrix. The driving force provided by boundary curvature is calculated to be 0.012 MPa. Therefore, a dislocation density difference of greater than $1.08\times10^{13}\ m^{-2}$ across the boundary is required for grain growth.

The initial dislocation density in the round grain is set to be $1\times10^{13}\ m^{-2}$, while it is $1.6\times10^{14}\ m^{-2}$ for the surrounding matrix. According to Eq. (20),

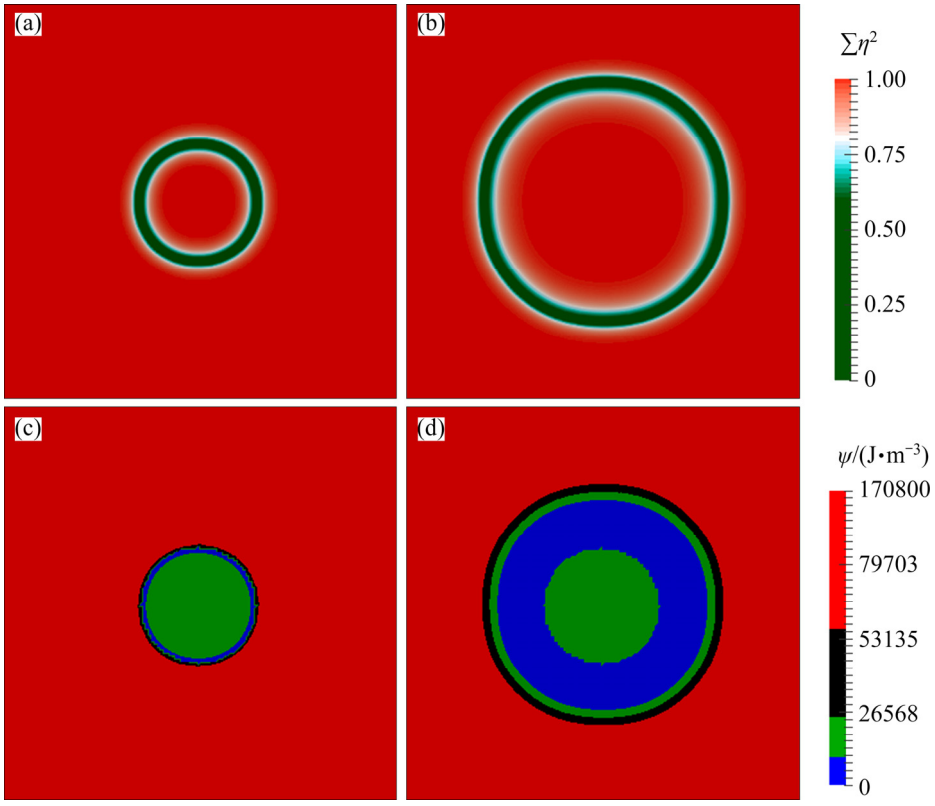

Fig. 4 Phase field model for bicrystal with circular boundary: (a) Initial configuration; (b) Configuration after grain growth; (c) Initial distribution of stored energy; (d) Distribution of stored energy after grain growth

the initial driving force for the grain boundary migration is 0.15 MPa. Dislocation density of the region swept by migrating boundaries is set to be a small value (0 m^{-2} in this work), which is consistent with the fact that area swept by the migrating boundaries is of low stored energy for SIBM [36]. The round grain will expand uniformly, with keeping a circular geometry during the phase field simulation (Fig. 4(b)), because every point on the grain boundary has the same driving force at any given moment.

The stored deformation energy provides much larger driving force than boundary curvature in current case. Moreover, the resistance force provided by the boundary curvature will become weaker as the grain radius increases, and the migration velocity will increase gradually. As shown in Fig. 5, the predicted migration velocities at different radius (empty circle) well match the theoretical results calculated from Eqs. (18)−(20) (curve) reasonably.

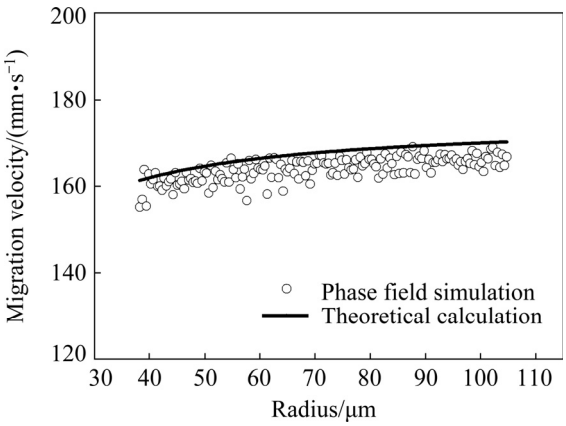

Fig. 5 Migration velocities from phase field simulations and theoretical calculations

3 Deformation and grain growth simulation of AA3102 aluminum alloy

In this section, the microstructure evolution during annealing of AA3102 after pre-strain is analyzed with current framework. The AA3102 aluminum alloy is firstly compressed at room temperature to different strains, and then annealed at 600 °C for various time periods. The predicted microstructure is compared with the experimental results for practical verification of the proposed models. One can refer to the previous work [7] for detailed experimental procedures. The effects of pre-strain and annealing process on the final microstructure are further discussed.

3.1 Model setup

3.1.1 Representative volume element (RVE) model

A 2D RVE including 100 grains is generated through Voronoi tessellation for CPFE model [37], as shown in Fig. 6(b). The RVE has an average grain size of 25 μm with random crystal orientations, which is consistent with the realistic microstructure (Fig. 6(a)). The RVE is discretized uniformly into 136×136 grid points along x and y directions, with a grid spacing of 1.824 μm. The RVE is modeled with eight-node continuum element by a reduced integration scheme (C3D8R). The uniaxial compression boundary condition is applied and solved with ABAQUS/standard software. A compressive displacement is assigned to the top surface to reach a total engineering strain of 1%, 5% and 10%, respectively, at a strain rate of 0.17 s^{-1}, while the bottom and left surfaces are

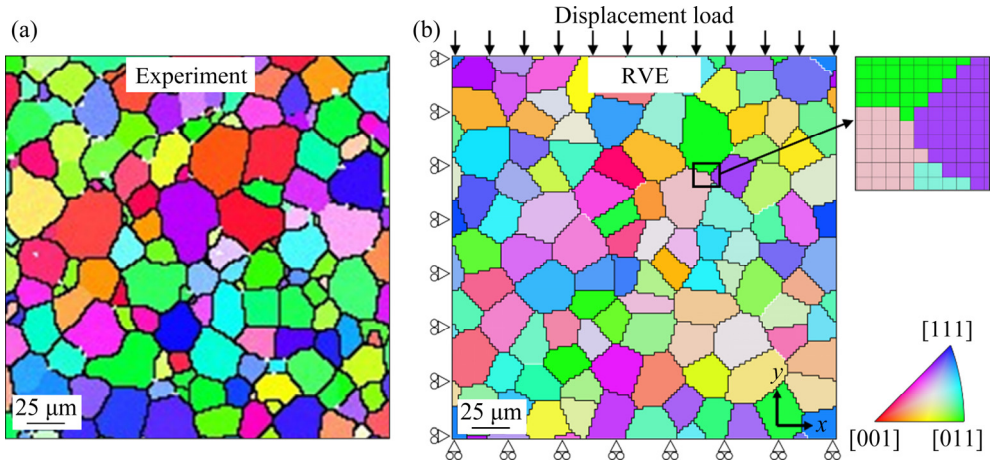

Fig. 6 Initial microstructure (a) and polycrystalline RVE (b) in CPFE model

constrained. A low initial dislocation density of 1.0×10^5 m^{-2} is assigned to the RVE model.

3.1.2 Static recrystallization nucleation and grain growth

The static softening process mainly involves static recovery (SRV), static recrystallization nucleation and growth of newly formed grains. The SRV in the alloy matrix reduces the driving force of grain boundary migration during the annealing process. Considering the dislocation density decreasing in the SRV process, an exponential function is adopted to model the dislocation density evolution [38]:

$$\rho(t)=\rho(t-\Delta t)\exp(-\lambda k_2\dot{\varepsilon}\Delta t) \tag{23}$$

where λ is a fitting parameter ranging from 0 to 1 (λ=0.15 in the present model), $\dot{\varepsilon}$ is the strain rate in previous deformation and Δt is the step length of annealing time and assigned with 0.05 s in the present model.

The actual nucleation process is a complicated thermal-activation process, which is mainly determined by the stored deformation energy induced during previous deformation. The nucleation rate of SRX ($\dot{n}$) can be calculated as [39,40]

$$\dot{n}=C\left(E_\mathrm{s}-E_0\right)V_\Omega\exp(-\frac{Q}{RT}) \tag{24}$$

where C is a model constant, E_s is the current stored energy and here simplified as average stored energy of RVE, E_0 is the critical stored deformation energy for nucleation, and V_Ω is the fraction of potential area for SRX. Equation (24) indicates that more nuclei will occur with higher stored energy. The number of nuclei in time period Δt can be calculated as

$$N_\mathrm{c}=\dot{n}S\Delta t \tag{25}$$

where S is the total area (or volume for 3D case) of the RVE. For simplification, the V_Ω is assigned with 1 constantly.

The main purpose of this work is to establish a novel framework by combing CPFE with PF to reproduce the strain induced abnormal grain growth process during annealing with various pre-strains. For SRX nucleation process, the heterogeneity in dislocation distribution in one grain is ignored for simplification purpose. Based on Eq. (25), N_c grains with average stored energy larger than E_0 are randomly selected as recrystallized nuclei and then their stored energy is reset to be zero. Those recrystallized grains can further grow up, driven by the difference of stored energy with their neighbors as well as grain boundary curvature.

3.2 Results and discussion

3.2.1 Mechanical responses

Figures 7(a_1, b_1, c_1) show the displacement maps along y direction after 1%, 5% and 10% compression strains, respectively, and a heterogeneous distribution is clearly observed due to different orientations and the corresponding deformations among the grains. Figures 7(a_2, b_2, c_2) present the distributions of dislocation density extracted from the CPFE simulations, where the overall dislocation density keeps increasing with the increase of deformation. Meanwhile, significant variations are observed among grains with different orientations. To illustrate the heterogeneous intragranular dislocation density distribution clearly, the dislocation density in one typical grain as marked with black arrows (Figs. 7(a_2, b_2, c_2)) is further plotted in Fig. 8.

3.2.2 Data mapping

The grid coordinates, crystal orientation and dislocation density calculated by CPFE analysis are transferred to phase filed model to simulate the grain nucleation and grain growth in the following annealing process. As the mesh structures in CPFE are unevenly deformed with the increase of strain, the data from CPFE are remapped through linear interpolation method before being transferred to phase filed. Figures 9 illustrates the polycrystalline structures (Figs. 9(a_1, b_1, c_1)) in PF and the corresponding distribution of stored deformation energy (Figs. 9(a_2, b_2, c_2)) at different compression strains.

A significantly heterogeneous distribution of stored deformation energy is observed in the polycrystalline RVE at different deformation stages. The heterogeneity in stored energy can generate the driving force for grain boundary migration, which causes the growth of grains with lower stored deformation energy at the expense of those with higher stored deformation energy. Such a driving force attempts to reduce the total free energy stored in the RVE.

3.2.3 Annealing simulation after pre-strain

Although the nucleation of SRX is a progressive process during the annealing treatment, the total number of nuclei is calculated at the beginning of the annealing simulation for

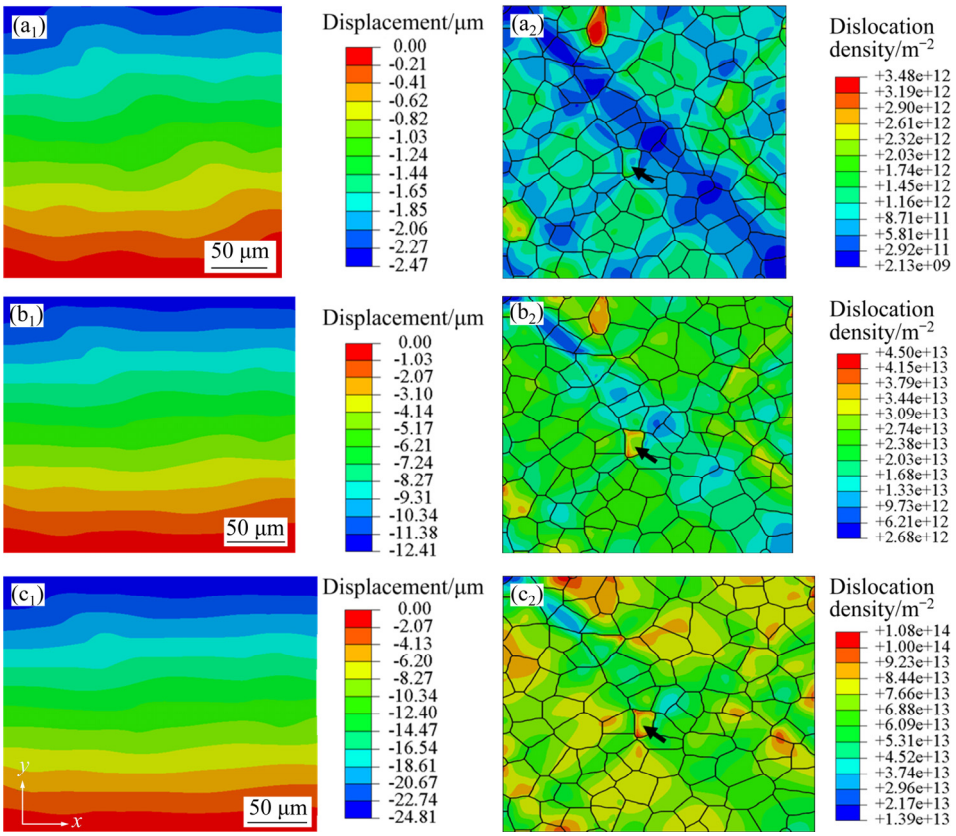

Fig. 7 Results from CPFE models: Displacement maps along y direction (a_1, b_1, c_1) and dislocation density distributions (a_2, b_2, c_2) after compression strains of 1% (a_1, a_2), 5% (b_1, b_2) and 10% (c_1, c_2)

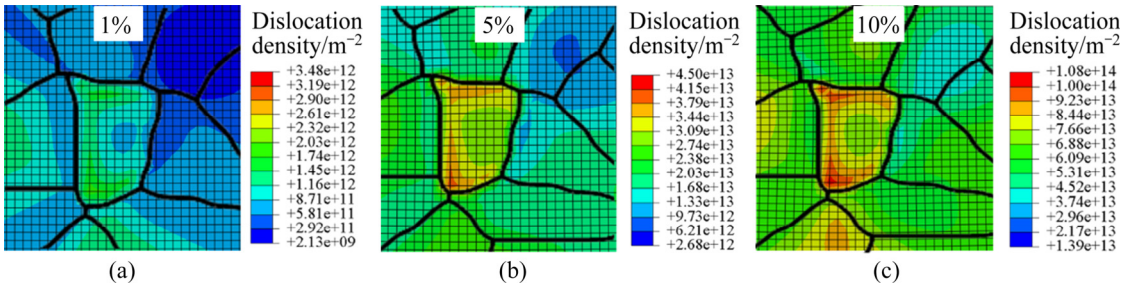

Fig. 8 Heterogeneous dislocation density distributions in one typical grain marked with black arrows in Fig. 7 at different compression strains

simplification purpose and the Δt in Eq. (25) is assigned with 180 s, which is the total annealing time. It is clearly observed that no SRX nucleation appears for 1% pre-strained case, since the stored energy is lower than the critical stored deformation energy E_0 (1.1×10^4 J·m^{-3}). The numbers of nuclei for 1%, 5% and 10% deformed alloys are 0, 2 and 10, respectively (Fig. 10).

The microstructure evolution of the annealing process from PF simulations and experiments are given in Fig. 11 and the average grain size is tracked in Fig. 12 for a quantitative illustration of grain growth. Distinctly different microstructures are obtained with various annealing time and pre-strains. Due to the lower stored deformation energy, there are no recrystallized nuclei formed in the 1% pre-strained alloy, as shown in Fig. 11(a). The deformed grains grow uniformly at a low velocity, driven by grain boundary energy and slight difference of stored energy between deformed grains. With more dislocations generated at larger deformation strain (10%), sufficient stored energy results in a higher nucleation rate and driving force for grain growth (Fig. 11(c)). A larger grain size is acquired after 180 s annealing, compared with that with 1% compression strain. However, a

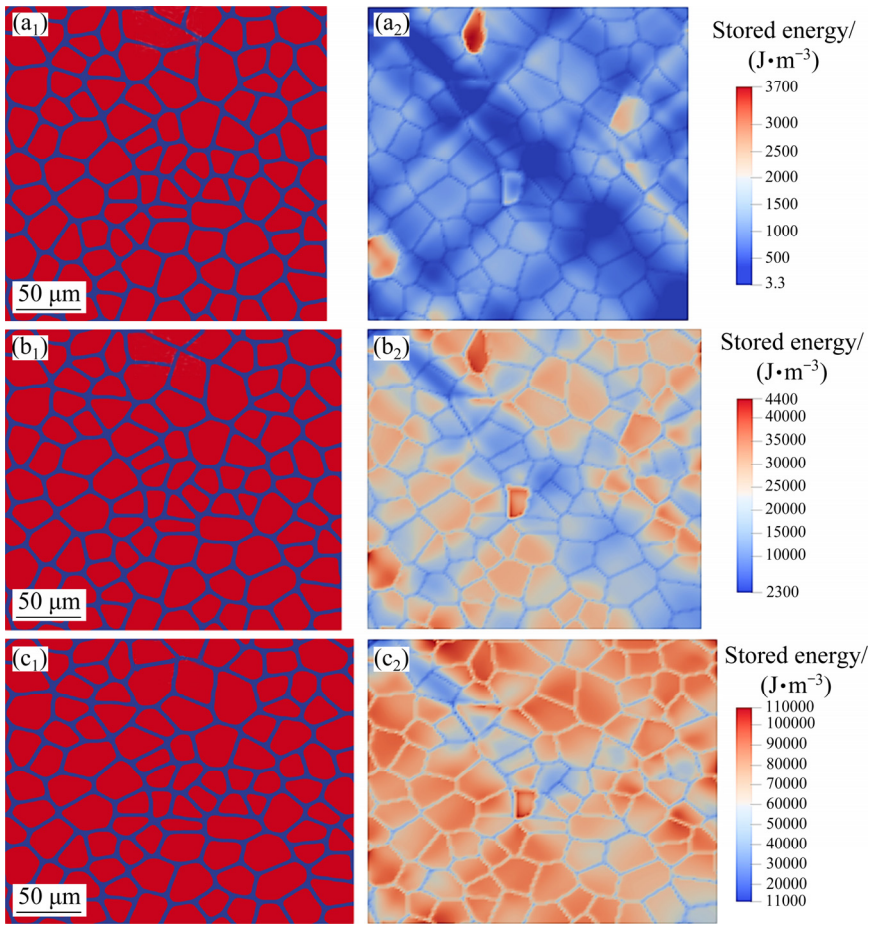

Fig. 9 Polycrystalline structures in PF (a_1, b_1, c_1) and stored energy distributions (a_2, b_2, c_2) after compression strains of 1% (a_1, a_2), 5% (b_1, b_2) and 10% (c_1, c_2)

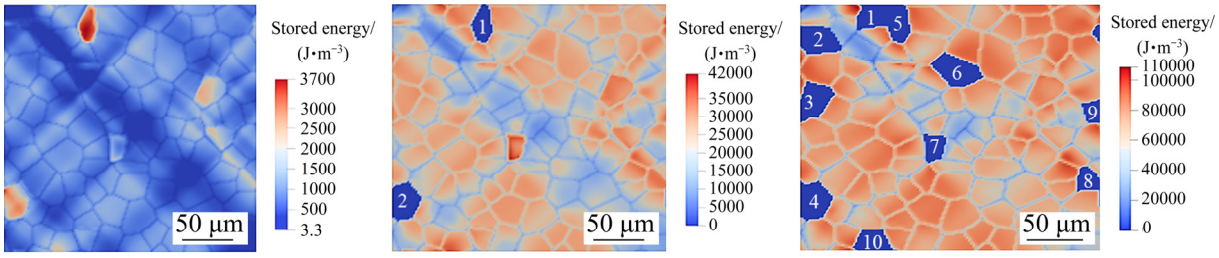

(a) (b) (c)

Fig. 10 Calculated nuclei with low stored energy after compression strains of 1% (a), 5% (b) and 10% (c)

significantly different microstructure is observed after the annealing at 5% pre-strain, as shown in Fig. 11(b). Abnormally large grains are reproduced in the AA3012 alloy at a medium plastic strain (5% compression strain in the present work). Two recrystallized nuclei with remarkably low stored energy are formed at the beginning and gradually encroach the deformed matrix with the increase of the annealing time. Although the average grain size in 5% pre-strain case increases with a lower velocity compared to that in 10% pre-strain case at the early stage, the SRX nuclei grow constantly till impinging each other, resulting in an abnormally large grain size. Hence, abnormally large (196 μm), medium (93 μm) and fine (43 μm) grain sizes are obtained for 5%, 10% and 1% pre-strain cases, respectively. The simulation results are well consistent with the experimental observations, which are given in Fig. 11 and Fig. 12. It is noted that the larger deviation of the final average grain size for 5% deformed alloys between simulated and experimental results in Fig. 12 should be attributed

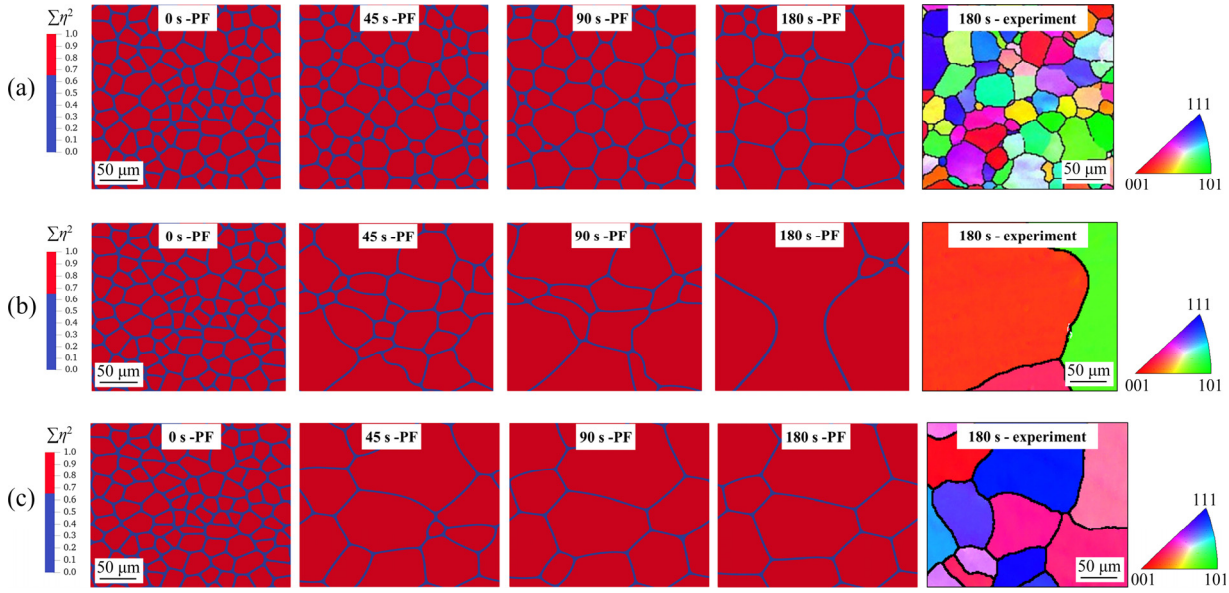

Fig. 11 Microstructure evolution from PF simulations and experiments with various annealing time after compression strains of 1% (a), 5% (b) and 10% (c)

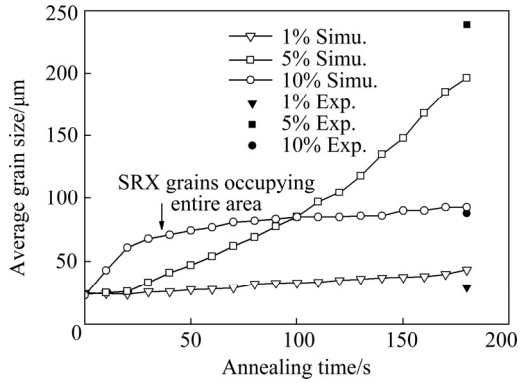

Fig. 12 Average grain size evolution with annealing time for different pre-strain cases

to the limitation of RVE size. When abnormal grain growth occurs, as Fig. 11(b) shows, no complete grain could be covered in this RVE due to the abnormally large grain size. Therefore, the average grain size may be underestimated. However, this will have little impact on the conclusions about the abnormal growth.

It is also worth noticing that the boundary migration shows a high velocity at the early stage of annealing for 10% pre-strain case. It demonstrates that recrystallized grains can consume the deformed matrix with a significant speed due to the remarkable stored energy difference as driving force. However, there is little increase in the average grain size after SRX grains occupy the entire area due to the much lower stored energy difference among the SRX grains. As shown in Fig. 13, the evolutions of stored deformation energy distribution at the early stage of annealing (0−45 s) are given to better illustrate the SRX growth driven by both stored energy and boundary curvature.

The present simulations support the conclusion that in the annealing of pre-strained AA3102 aluminum alloy, there is a critical plastic strain for abnormally grain growth, at which a limited number of SRX nuclei are formed and grow into abnormally large grains at the expense of deformed matrix [7].

4 Conclusions

(1) A framework coupling crystal plasticity and phase field methods is proposed to simulate the microstructure evolution in the annealing of deformed aluminum alloy. A dislocation density-based crystal plasticity finite element model is adopted to predict the stored deformation energy evolution during plastic deformation and the phase field to simulate the strain induced grain growth in following annealing process. The simulation results are in good agreement with the experimental observations.

(2) Both inter-granular and intra-granular heterogeneities of dislocation density in different deformation stages are captured by the crystal plasticity model. Higher stored deformation energy is generated with the increase of plastic strain,

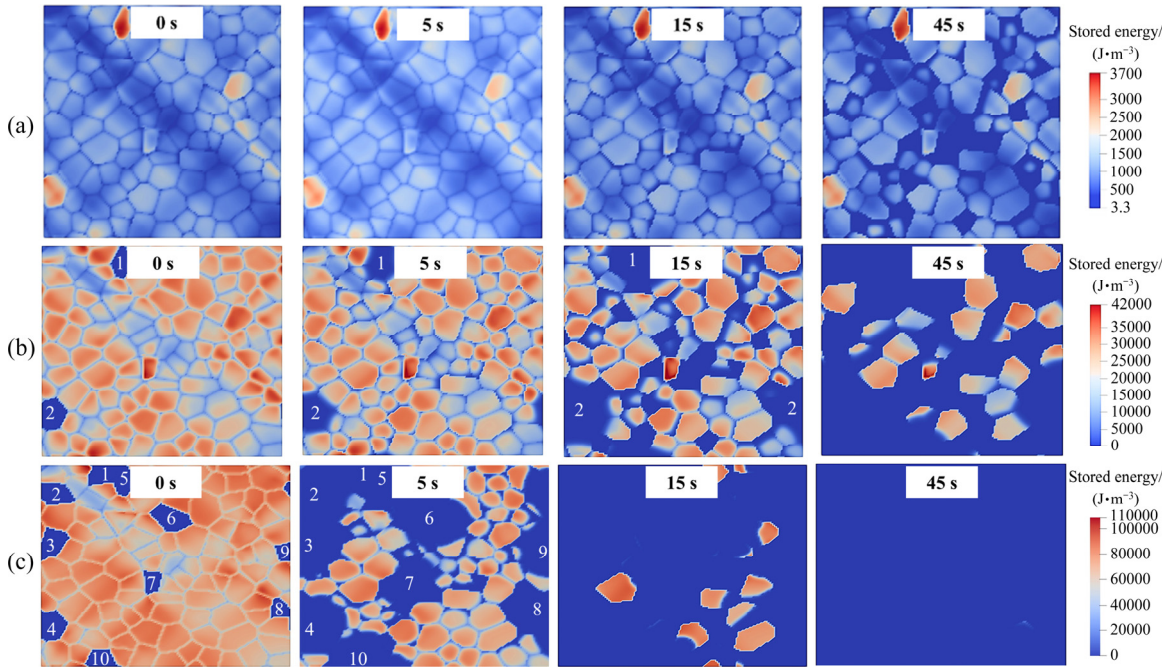

Fig. 13 Stored deformation energy distributions at early stage of annealing for various pre-strain cases: (a) 1%; (b) 5%; (c) 10%

resulting in more SRX nuclei during annealing process.

(3) The driving forces arise from both stored deformation energy and local boundary curvature in the extended continuum-field model. The nuclei with low stored energy embedded within deformed matrix tend to grow up, and abnormal large grains occur when the pre-strain is close to the critical plastic strain, attributing to the limited number of recrystallized nuclei and stored energy heterogeneity.

(4) The established approach can also be extended to simulate grain structure evolution of a 3D polycrystalline microstructure, through which more details on the grain growth in metals may be explored.

Appendix

Appendix in this work can be found at: http://tnmsc.csu.edu.cn/download/03-p3873-2021-1041-Appendix.pdf.

Acknowledgments

The authors acknowledge the financial support from the National Natural Science Foundation of China (Nos. U2141215, 52105384 and 52075325). Dr. LI thanks the support of Materials Genome Initiative Center, Shanghai Jiao Tong University, China.

References

[1] LENG Jin-feng, REN Bing-hui, ZHOU Qing-bo, ZHAO Ji-wei. Effect of Sc and Zr on recrystallization behavior of 7075 aluminum alloy [J]. Transactions of Nonferrous Metals Society of China, 2021, 31(9): 2545−2557.

[2] QUAN Guo-zheng, ZHANG Pu, MA Yao-yao, ZHANG Yu-qing, LU Chao-long, WANG Wei-yong. Characterization of grain growth behaviors by BP-ANN and Sellars models for nickle-base superalloy and their comparisons [J]. Transactions of Nonferrous Metals Society of China, 2020, 30(9): 2435−2448.

[3] SAITO G, ZHANG T, SAKAGUCHI N, OHNO M, MATSUURA K, TAKEUCHI M, SANO T, MINOGUCHI K, YAMAOKA T. In-situ observation of abnormal grain growth in a low-alloyed carbon steel using SEM-EBSD [J]. Materialia, 2021, 15: 100985.

[4] KIM H C, KANG C G, HUH M Y, ENGLER O. Effect of primary recrystallization texture on abnormal grain growth in an aluminum alloy [J]. Scripta Materialia, 2007, 57(4): 325−327.

[5] NA T W, PARK H K, PARK C S, PARK J T, HWANG N M. Misorientation angle analysis near the growth front of abnormally growing grains in 5052 aluminum alloy [J]. Acta Materialia, 2016, 115: 224−229.

[6] VYSOTSKIY I, MALOPHEYEV S, MIRONOV S, KAIBYSHEV R. Effect of pre-strain path on suppression of abnormal grain growth in friction-stir welded 6061 aluminum alloy [J]. Materials Science and Engineering A, 2019, 760(4): 206−213.

[7] LI Kai, ZOU Tian-xia, LI Da-yong, PENG Ying-hong, SHU Da. On formation of abnormally large grains in annealing

prestrained aluminum alloy multiport extrusion tubes [J]. Metallurgical and Materials Transactions A, 2019, 50(12): 5734−5749.

[8] WANG Xiang-dong, LIU Xiong, DING Hao, YAN Su-rong, XIE Zi-hua, PAN Bai-qing, LI Yong-hong, PAN Qing-lin, DENG Yun-lai, WANG Wei-yi. Microstructure and mechanical properties of Al−Mg−Si alloy U-shaped profile [J]. Transactions of Nonferrous Metals Society of China, 2020, 30(11): 2915−2926.

[9] LU N, KANG J, SENABULYA N, KEINAN R, GUENINCHAULT N, SHAHANI A. Dynamics of particle-assisted abnormal grain growth revealed through integrated three-dimensional microanalysis [J]. Acta Materialia, 2020, 195: 1−12.

[10] YANG Shui-yuan, QING Xin-yu, ZHANG Ji-xun, GUO Li-peng, HONG Shen, LI Meng-pei, ZHANG Jin-bin, WANG Cui-ping, LIU Xing-jun. Role of β(FeAl) nano-particles in abnormal grain growth in the annealing of cast Cu−Al−Mn−Fe shape memory alloys [J]. Progress in Natural Science: Materials International, 2020, 30(4): 510−516.

[11] JAFARI M, JAMSHIDIAN M, ZIAEI-RAD S, RAABE D, ROTERS F. Constitutive modeling of strain induced grain boundary migration via coupling crystal plasticity and phase-field methods [J]. International Journal of Plasticity, 2017, 99: 19−42.

[12] JIN S, KANG B, KONG T, HONG S H, SHIN H J, RUOFF R S. Strain-induced abnormal grain growth of Fe foils [J]. Journal of Alloys and Compounds, 2021, 853: 157390.

[13] ROTERS F, EISENLOHR P, HANTCHERLI L, TJAHJANTO D D, BIELER T R, RAABE D. Overview of constitutive laws, kinematics, homogenization and multiscale methods in crystal plasticity finite-element modeling: Theory, experiments, applications [J]. Acta Materialia, 2010, 58(4): 1152−1211.

[14] JAFARI M, SAEIDI N, ZIAEI-RAD S, JAMSHIDIAN M, KIM H S. Micromechanical analysis of orientation dependency on deformation behavior in DP steels by dislocation density-based crystal plasticity simulation [J]. Mechanics of Materials, 2019, 134(3): 132−142.

[15] ARDELJAN M, BEYERLEIN I J, KNEZEVIC M. A dislocation density based crystal plasticity finite element model: Application to a two-phase polycrystalline HCP/BCC composites [J]. Journal of the Mechanics and Physics of Solids, 2014, 66(1): 16−31.

[16] MA A, ROTERS F, RAABE D. Studying the effect of grain boundaries in dislocation density based crystal-plasticity finite element simulations [J]. International Journal of Solids and Structures, 2006, 43(24): 7287−7303.

[17] LIU Lei, WU Yun-xin, AHMAD A S. A novel simulation of continuous dynamic recrystallization process for 2219 aluminium alloy using cellular automata technique [J]. Materials Science and Engineering A, 2021, 815: 141256.

[18] EIVANI A R, JAFARIAN H R, ZHOU J. Simulation of peripheral coarse grain structure during hot extrusion of AA7020 aluminum alloy [J]. Journal of Manufacturing Processes, 2020, 57(4): 881−892.

[19] LUAN Qin-meng, LEE J, ZHENG Ze-bang, LIN Jian-guo, JIANG Jun. Static recrystallization study on pure aluminium using crystal plasticity finite element and phase-field modelling [J]. Procedia Manufacturing, 2018, 15: 1800−1807.

[20] STEINBACH I, PEZZOLLA F, NESTLER B, SEEBELBERG M, PRIELER R, SCHMITZ G J, REZENDE J L L. A phase field concept for multiphase systems [J]. Physica D: Nonlinear Phenomena, 1996, 94(3): 135−147.

[21] CHEN Long-qing, YANG Wei. Computer simulation of the domain dynamics of a quenched system with a large number of nonconserved order parameters: The grain-growth kinetics [J]. Physical Review B, 1994, 50(21): 15752−15756.

[22] FAN Da-nan, CHEN Long-qing. Diffusion-controlled grain growth in two-phase solids [J]. Acta Materialia, 1997, 45(8): 3297−3310.

[23] ABRIVARD G, BUSSO E P, FOREST S, APPOLAIRE B. Phase field modelling of grain boundary motion driven by curvature and stored energy gradients. Part I: Theory and numerical implementation [J]. Philosophical Magazine, 2012, 92(28/29/30): 3618−3642.

[24] GÜVENÇ O, BAMBACH M, HIRT G. Coupling of crystal plasticity finite element and phase field methods for the prediction of SRX kinetics after hot working [J]. Steel Research International, 2014, 85(6): 999−1009.

[25] TAKAKI T, TOMITA Y. Static recrystallization simulations starting from predicted deformation microstructure by coupling multi-phase-field method and finite element method based on crystal plasticity [J]. International Journal of Mechanical Sciences, 2010, 52(2): 320−328.

[26] JAFARI M, JAMSHIDIAN M, ZIAEI-RAD S, LEE B J. Modeling length scale effects on strain induced grain boundary migration via bridging phase field and crystal plasticity methods [J]. International Journal of Solids and Structures, 2019, 174/175: 38−52.

[27] ZHAO L, CHAKRABORTY P, TONKS M R, SZLUFARSKA I. On the plastic driving force of grain boundary migration: A fully coupled phase field and crystal plasticity model [J]. Computational Materials Science, 2017, 128: 320−330.

[28] MARIN E B, DAWSON P R. On modelling the elasto-viscoplastic response of metals using polycrystal plasticity [J]. Computer Methods in Applied Mechanics and Engineering, 1998, 165(1/2/3/4): 1−21.

[29] HUTCHINSON J W. Bounds and self-consistent estimates for creep of polycrystalline materials [J]. Proceedings of the Royal Society of London. A. Mathematical and Physical Sciences, 1976, 348(1652): 101−127.

[30] KOCKS U F, MECKING H. Physics and phenomenology of strain hardening: The FCC case [J]. Progress in Materials Science, 2003, 48: 171−273.

[31] BEYERLEIN I J, TOMÉ C N. A dislocation-based constitutive law for pure Zr including temperature effects [J]. International Journal of Plasticity, 2008, 24(5): 867−895.

[32] ZHOU Guo-wei, LI Zi-han, LI Da-yong, PENG Ying-hong, ZUROB S H, WU Pei-dong. A polycrystal plasticity based discontinuous dynamic recrystallization simulation method and its application to copper [J]. International Journal of Plasticity, 2017, 91: 48−76.

[33] CHEN S F, LI D Y, ZHANG S H, HAN H N, LEE H W, LEE M G. Modelling continuous dynamic recrystallization of aluminum alloys based on the polycrystal plasticity approach

[J]. International Journal of Plasticity, 2020, 131: 102710.
[34] MOELANS N, BLANPAIN B, WOLLANTS P. Quantitative analysis of grain boundary properties in a generalized phase field model for grain growth in anisotropic systems [J]. Physical Review B, 2008, 78(2): 024113.
[35] ZHANG Tao, LU Shi-hong, WU Yun-xin, GONG Hai. Optimization of deformation parameters of dynamic recrystallization for 7055 aluminum alloy by cellular automaton [J]. Transactions of Nonferrous Metals Society of China, 2017, 27(6): 1327−1337.
[36] BECK P A, SPERRY P R. Strain induced grain boundary migration in high purity aluminum [J]. Journal of Applied Physics, 1950, 21(2): 150−152.
[37] WERNER E, SIEGMUND T, WEINHANDL H, FISCHER F D. Properties of random polycrystalline two-phase materials [J]. Applied Mechanics Reviews, 1994, 47(1): 231−240.
[38] KUGLER G, TURK R. Modeling the dynamic recrystallization under multi-stage hot deformation [J]. Acta Materialia, 2004, 52(15): 4659−4668.
[39] IVASISHIN O M, SHEVCHENKO S V, VASILIEV N L, SEMIATIN S L. A 3-D Monte−Carlo (Potts) model for recrystallization and grain growth in polycrystalline materials [J]. Materials Science and Engineering A, 2006, 433: 216−232.
[40] CHEN Fei, CUI Zhen-shan. Mesoscale simulation of microstructure evolution during multi-stage hot forging processes [J]. Modelling and Simulation in Materials Science and Engineering, 2012, 20(4): 045008.

铝合金应变诱导晶粒异常长大行为的晶体塑性−相场法耦合模拟

刘如学[1]，李 凯[1]，周国伟[2]，唐伟琴[1]，沈 耀[3]，唐 鼎[1]，李大永[1]

1. 上海交通大学 机械与动力工程学院，上海 200240；
2. 上海交通大学 船舶海洋与建筑工程学院，上海 200240；
3. 上海交通大学 材料科学与工程学院，上海 200240

摘 要：提出一种预测变形铝合金在退火过程中应变诱导晶粒异常长大行为的介观耦合建模方法。基于晶体塑性有限元法(CPFE)计算塑性变形中的位错密度和变形储能分布；以储能和局部界面曲率为晶界迁移驱动力，建立基于连续场法的改进相场(PF)模型，并采用插值法将 CPFE 计算结果向 PF 模型进行映射，实现 CPFE−PF 的耦合模拟。采用理想双晶组织模拟初步校准 PF 模型，然后将该 CPFE−PF 耦合模型应用于变形 AA3102 铝合金退火过程的多晶组织演化模拟，进一步验证模型有效性。结果表明，退火时变形基体中的低储能形核点优先长大；而当变形量在临界塑性应变附近时，由于结晶形核数量的有限性和储能分布的不均匀性，将产生晶粒异常长大现象。

关键词：晶粒异常长大；储存变形能；再结晶；晶体塑性；相场

(Edited by Wei-ping CHEN)